

# External tissue support and fluid–structure simulation in blood flows

P. Moireau · N. Xiao · M. Astorino · C. A. Figueroa ·  
D. Chapelle · C. A. Taylor · J.-F. Gerbeau

Received: 26 August 2010 / Accepted: 13 January 2011 / Published online: 10 February 2011  
© Springer-Verlag 2011

**Abstract** The objective of this work is to address the formulation of an adequate model of the external tissue environment when studying a portion of the arterial tree with fluid–structure interaction. Whereas much work has already been accomplished concerning flow and pressure boundary conditions associated with truncations in the fluid domain, very few studies take into account the tissues surrounding the region of interest to derive adequate boundary conditions for the solid domain. In this paper, we propose to model the effect of external tissues by introducing viscoelastic support conditions along the artery wall, with two—possibly distributed—parameters that can be adjusted to mimic the response of various physiological tissues. In order to illustrate the versatility and effectiveness of our approach, we apply this strategy to perform patient-specific modeling of thoracic aortae based on clinical data, in two different cases and using a distinct fluid–structure interaction methodology for each, namely an Arbitrary Lagrangian–Eulerian (ALE) approach with prescribed inlet motion in the first case and the coupled momentum method in the second case. In both

cases, the resulting simulations are quantitatively assessed by detailed comparisons with dynamic image sequences, and the model results are shown to be in very good adequacy with the data.

**Keywords** Blood flows · Boundary conditions · Tissue support · Fluid-structure interaction · Aorta modeling · Patient-specific geometry

## 1 Introduction

Fluid–structure interaction (FSI) in arteries has been addressed in numerous works during the last decade. With a view to performing meaningful and accurate simulations in a clinically relevant timeframe—and for patient-specific modeling, in particular—it is currently unfeasible to consider the entire arterial tree when modeling three-dimensional blood flows in compliant arteries. Therefore, artificial truncations must be introduced in the computational domains and some adequate boundary conditions considered. In the blood flow domain, much work has already been accomplished concerning flow and pressure boundary conditions. For example, as advocated in [Formaggia et al. \(2001\)](#), the three-dimensional FSI problem can be coupled to a one-dimensional hyperbolic system to obtain appropriate boundary conditions. This study was further extended in [Formaggia et al. \(2007\)](#) and similar ideas can be found in [Vignon-Clementel et al. \(2006\)](#), [Blanco et al. \(2007\)](#), [Blanco et al. \(2009\)](#), and [Papadakis \(2009\)](#) using one-dimensional or ordinary differential equations models for the downstream flows. However, notwithstanding these artificial boundaries, regarding the *natural boundaries* on the vessel walls, few approaches take into account the tissues surrounding the region of interest to derive adequate boundary conditions for the vessel wall domain. In fact, in all the FSI studies we are aware of, a constant—frequently zero—

---

P. Moireau (✉) · M. Astorino · D. Chapelle · J.-F. Gerbeau  
INRIA Paris-Rocquencourt, B.P.105, 78153 Le Chesnay, France  
e-mail: philippe.moireau@inria.fr

P. Moireau · N. Xiao · C. A. Figueroa · C. A. Taylor  
Department of Bioengineering, Stanford University, Clark Center,  
318 Campus Drive, Stanford, CA 94305-5431, USA

J.-F. Gerbeau  
Department of Mechanical Engineering (Visiting),  
Stanford University, 440 Escondido Mall,  
Stanford, CA 94305-3030, USA

### Present Address:

M. Astorino  
Chair of modelling and Scientific Computing, Ecole Polytechnique  
Fédérale de Lausanne, Station 8-MA, 1015 Lausanne, Switzerland

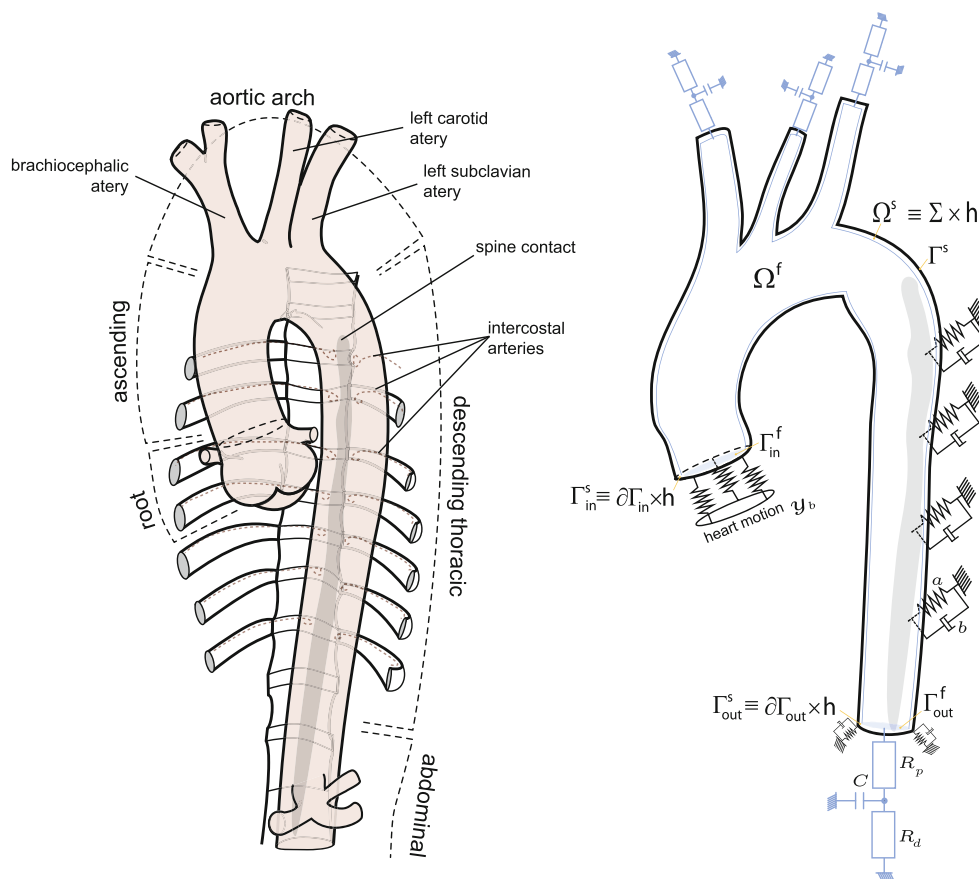


**Fig. 1** Schematic representation of aorta and its surrounding organs. Model domain and boundary conditions

pressure is applied on the outer part of the artery wall. This simple boundary condition is not able to sustain the artery and typically results in artificial motion patterns of the arterial wall. In practice, this motion induces inaccuracies much greater than those introduced by spurious reflections on artificial boundaries. It is of course out of the question to model in detail the organs surrounding the vessels. Another option could be to directly prescribe displacements inferred from the image sequence as time-dependent Dirichlet boundary conditions. However, this approach would directly be impacted by the noise contained in the data sequence—especially regarding the time sampling. Furthermore, such an *image-driven* fluid model would have a quite limited predictive character, as for example some fast wave propagation phenomena in the arteries—or various hemodynamic states without prior corresponding imaging—could not be described.

By contrast, in this paper, we introduce boundary conditions along the artery wall that consist of a viscoelastic term representing the support provided by the surrounding tissues. We show that this simple model corresponds to a generalized Robin boundary condition on the walls. It relies on two parameters, possibly distributed, that can be adjusted to mimic the response of various physiological tissues.

In order to illustrate the versatility of this approach, we will demonstrate its effectiveness for two classes of FSI models. In the first model, the motion of the blood flow domain is handled through an Arbitrary Lagrangian–Eulerian (ALE) formulation and the structure is nonlinear. In the second model, we use the coupled momentum method—introduced in [Figueroa et al. \(2006\)](#)—by which the blood flow domain is assumed to be fixed and the structure is modeled as a linear elastic membrane. In both cases, we have focused our attention on the thoracic aorta, since it can undergo large displacements and experiences a complex coupling with surrounding organs, namely interactions with the spine on the outer wall and with the heart in the ascending thoracic aorta (see [Fig. 1](#)), in particular.

The outline of this paper is as follows. After presenting the clinical data—and the image processing techniques—on which the subsequent patient-specific modeling is based, we introduce the fluid–structure modeling formulations in [Sect. 3](#), with an emphasis on the specific boundary conditions proposed for representing the effect of external tissues on blood vessels, in particular for the aorta. Then, in [Sect. 4](#), we present detailed simulation results for two clinical examples modeled with the two aforementioned FSI formu-

lations. Finally, in Sect. 5, we discuss these results based on a comparison of the computed wall motion—with and without the external tissue support conditions—with the motion observed in the medical imaging data. We finally give some concluding remarks in Sect. 6.

## 2 Cardiovascular data

*Image data.* Two subjects were selected for this study: the first subject is a 37-year-old man with significant thoracic aorta wall motion, whereas the second subject is a 59-year-old man with relatively small thoracic aorta wall motion. Informed consent was obtained from each subject, and all imaging protocols were approved by the Institutional Review Board. Medical data of the chest anatomy were obtained using a 64-row multidetector computed tomography (CT) scanner (Somatom Sensation Cardiac 64, Siemens Medical Solutions). Ten phases were reconstructed through the cardiac cycle with a temporal resolution of 164 milliseconds. For the 37-year-old man, each phase consists of a  $512 \times 512 \times 299$  voxel image, with an in-plane resolution of  $0.62 \times 0.62$  mm and a slice thickness of 1.00 mm. The display field of view (DFOV) is  $31.6 \times 31.6$  cm. For the 59-year-old man, each phase consists of a  $512 \times 512 \times 395$  voxel image, with an in-plane resolution of  $0.7 \times 0.7$  mm and a slice thickness of 0.7 mm. The DFOV is  $35.9 \times 35.9$  cm. The ten-phase cardiac-gated computed tomography (CT) data provide a description of the arterial lumen motion for the main vessels in the chest, namely the ascending aorta, aortic arch, descending aorta, brachiocephalic trunk, left carotid, and left subclavian arteries, as well as the intercostal arteries.

Figure 2 depicts the methodology used to generate a computer model of the thoracic aorta: starting with the phase of the cardiac-gated CT data corresponding to diastole, a 3D segmentation is performed using a level-set method (Yushkevich et al. 2006; Xiong et al. 2010). A triangular surface mesh is then generated, followed by the trimming of the inlet and outlet branches to generate flat surfaces suitable for boundary condition specification in the flow domain. Lastly, the flow domain is discretized into a  $\mathbb{P}_1$ -Lagrange tetrahedral finite element mesh. In the case of the Arbitrary Lagrangian–Eulerian FSI model, a solid mesh consisting of linear tetrahedra is generated by extruding the triangular surface mesh of the flow domain. The solid mesh is divided into regions associated with different material parameters for the viscoelastic external tissue boundary condition representing the effect of the different tissues and organs on the thoracic aorta.

Once we have defined the (time-dependent) domain of interest using the cardiac-gated CT data, we must obtain additional information concerning blood flow and pressure to define boundary conditions for the FSI problems.

*Boundary condition data for the blood flow domain.* Unlike other medical imaging modalities such as Doppler ultra-

sound and phase-contrast magnetic resonance imaging (PC-MRI) that enable non-invasive measurement of blood flow (Taylor and Figueroa 2009), CT data do not provide velocity information. We must therefore resort to using blood flow data that in general is not recorded simultaneously with the CT data. Conventionally, a flow or pressure waveform obtained in a separate measurement has been utilized to define a Dirichlet inflow boundary condition for the flow domain. More recently, lumped-parameter models representing the interactions of the heart with the aorta have been proposed in a multiscale (or multidimensional) approach to boundary condition specification (Sainte-Marie et al. 2006; Kerckhoffs et al. 2007; Kim et al. 2009). In this work, we have assumed a flow waveform measured at the level of the aortic root and mapped to a flat velocity profile on the inlet face of the model. Here, special care must be taken in ensuring that the flow waveform is synchronized with the phases of the cardiac-gated CT data to avoid spurious modes induced by inconsistent boundary conditions in the FSI simulations.

Accurate recording of blood pressure data is generally a difficult task. Usually, non-invasive discrete measurements of brachial systolic and diastolic blood pressures are taken using an automatic pressure cuff. Transfer functions can be utilized to extrapolate these peripheral measurements to central aortic pressure values (Chen et al. 1997). Continuous measurement of blood pressure is a more complex procedure: radial artery tonometry can be used to perform continuous non-invasive arterial pressure measurements with limited accuracy (Weiss et al. 1996), whereas pressure transducers are used to accurately measure continuous pressure invasively.

The outflow faces of the cardiovascular model are usually chosen to specify a boundary condition on the total or normal traction of the blood flow domain. We have utilized a 3-element Windkessel lumped-parameter model coupled to the outlet faces of the blood flow domain via a weak traction boundary condition. This lumped-parameter model defines a proximal resistance  $R_p$ , a capacitance  $C$ , and a distal resistance  $R_d$  to represent the characteristics of the distal vasculature not included in the 3D computational domain. More details on the specification of the boundary conditions parameters for the blood flow domain are given in Sect. 3.2.1.

*Boundary condition data for the vessel wall domain.* Unlike the flat faces of the blood flow domain that represent *artificial* boundaries, the boundary along the outer part of the vessel walls represents a *natural* boundary for the FSI domain. In this paper, we use a generalized Robin boundary condition to represent the viscoelastic behavior of the tissues surrounding the thoracic aorta. This boundary condition introduces a relation between the stress, the displacement and the velocity. For the Arbitrary Lagrangian–Eulerian FSI model, we account for the large motion

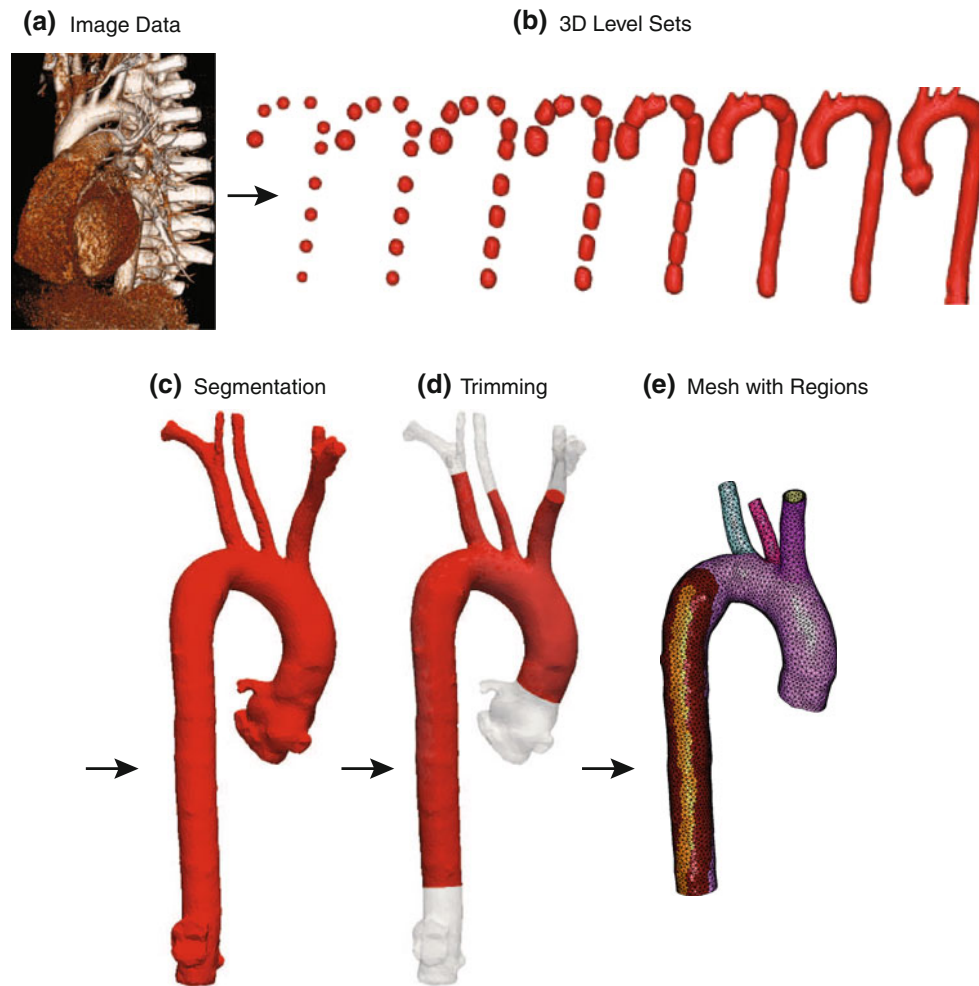


**Fig. 2** Mesh construction from cardiovascular image data. **a** Volume rendering of image containing one phase of the cardiac-gated CT data. **b** 3D level set is grown to detect the lumen boundaries. **c** Segmentation shows the reconstruction of the domain of interest in the ascending aorta. **d** Trimming of the segmentation produces flat inlet and outlet

faces better suitable for boundary condition specification in the blood flow domain. **e** Vessel wall mesh showing the regions considered for assigning different material parameter values for the viscoelastic boundary condition

experienced by the root of the thoracic aorta by using a Robin boundary condition where a displacement field  $\underline{y}_b$  is weakly enforced for the nodes in the proximal boundary of the vessel wall domain. The displacement  $\underline{y}_b$  can be estimated from the ten phases of the cardiac-gated CT data. Lastly, boundary conditions are required for the vessel wall boundaries on the outflow branches of the model. Traditionally, homogeneous Dirichlet conditions are employed in these boundaries, but this approach presents a major drawback in that it may generate non-physiological reflections and high-frequency vibrations in the vessel wall. In this work, we propose to also use a Robin boundary condition on these boundaries to model the rest of the arterial tree in a more natural way. Details on the formulation of the boundary conditions for the vessel wall domain are given in Sect. 3.2.2.

### 3 Models

#### 3.1 General modeling considerations

In this section, we sketch the derivation of the fundamental law of dynamics—and the associated principle of virtual work—in a total Lagrangian framework, with the primary objective of introducing the required notation. The main domain definitions are indicated in Fig. 1.

##### 3.1.1 Kinematics

Let  $\Omega(t)$  be a time-dependent domain in  $\mathbb{R}^3$  with  $t \in [0, T]$  the interval of a cardiac cycle ( $T \simeq 1$ s in humans). We assume, for all time  $t$ , that  $\overline{\Omega(t)} = \overline{\Omega^f(t)} \cup \overline{\Omega^s(t)}$  and  $\Omega^f(t) \cap \Omega^s(t) = \emptyset$ , where  $\Omega^f(t)$  is occupied by an

incompressible viscous fluid (i.e., the blood) and  $\Omega^s(t)$  by a viscoelastic solid (i.e., the vessel wall). The fluid–structure interface is denoted by  $\Sigma(t) = \overline{\Omega^f(t)} \cap \overline{\Omega^s(t)}$ , and the thickness of the vessel wall domain is denoted by  $h$ , which can be a function of space. By a slight abuse of notation, we may denote the vessel wall domain as  $\Omega^s(t) = \Sigma(t) \times h$ .

Let  $\Omega_0 = \Omega_0^f \cup \Omega_0^s$  be a reference configuration for the system. We denote the deformation of the solid medium by

$$\phi_s : \Omega_0^s \times [0, T] \longrightarrow \Omega^s(t),$$

$$\phi_s : (\underline{\xi}, t) \longmapsto \underline{x} = \underline{\phi}_s(\underline{\xi}, t)$$

The displacement of the domain is given by  $\underline{y}_s(\underline{\xi}, t) \stackrel{\text{def}}{=} \underline{\phi}_s(\underline{\xi}, t) - \underline{\xi}$ . Within the solid domain, the velocity of a material point  $\underline{\xi}$ ,  $\partial_t \underline{\phi}_s(\underline{\xi}, t) = \partial_t \underline{y}_s(\underline{\xi}, t)$ , is denoted by  $\underline{u}_s$ . We then introduce the deformation gradient

$$\underline{F}_s(\underline{\xi}, t) \stackrel{\text{def}}{=} \underline{\nabla}_{\underline{\xi}} \underline{\phi}_s(\underline{\xi}, t),$$

such that any local variation of the volume of the domain is given by  $J_s(\underline{\xi}, t) \stackrel{\text{def}}{=} \det \underline{F}_s(\underline{\xi}, t)$ . Let us finally introduce the linearized Green–Lagrange tensor

$$\underline{\varepsilon}(\underline{y}_s) \stackrel{\text{def}}{=} \frac{1}{2} \left( \underline{\nabla}_{\underline{\xi}} \underline{y}_s + \underline{\nabla}_{\underline{\xi}} \underline{y}_s^T \right),$$

in other words, the symmetrized gradient, which also gives the strain rate tensor when applied to a velocity field. In fact, we will mainly use the strain rate for the fluid velocity field denoted by  $\underline{u}_f$  and defined by differentiating with respect to the Eulerian frame, namely

$$\underline{\varepsilon}(\underline{u}) = \frac{1}{2} \left( \underline{\nabla}_{\underline{x}} \underline{u} + \underline{\nabla}_{\underline{x}} \underline{u}^T \right).$$

### 3.1.2 Fundamental law of dynamics

Any continuum mechanics system—fluid or solid—satisfies the fundamental law of dynamics

$$\rho \underline{\gamma} - \text{div}_{\underline{x}} \underline{\sigma} = \rho \underline{f}, \text{ in } \Omega(t) \tag{1}$$

where  $\underline{\sigma}$  denotes the Cauchy stress tensor,  $\underline{f}$  is a volume-distributed force per unit mass,  $\rho$  the mass per unit volume, and  $\underline{\gamma} = \frac{d\underline{u}}{dt}$  where  $\frac{d}{dt}$  corresponds to the total derivative with respect to time. From a variational standpoint, the fundamental law of dynamics gives then—using the symmetry of the Cauchy stress tensor—the so-called principle of virtual work

$$\forall \underline{v} \in \mathcal{V}, \int_{\Omega(t)} \rho \underline{\gamma} \cdot \underline{v} \, d\Omega + \int_{\Omega(t)} \underline{\sigma} : \underline{\varepsilon}(\underline{v}) \, d\Omega$$

$$= \int_{\Omega(t)} \rho \underline{f} \cdot \underline{v} \, d\Omega + \int_{\Gamma_N(t)} \underline{t} \cdot \underline{v} \, dS, \tag{2}$$

where  $\underline{t}$  denotes a surface-distributed traction load on the boundary of the domain  $\Gamma_N(t) \subset \partial\Omega(t)$  where natural

conditions apply, and  $\mathcal{V}$  is the space of admissible virtual displacements taking into account the essential boundary conditions. If we choose to express this formulation in the reference configuration, we classically introduce the first Piola–Kirchhoff stress tensor

$$\underline{\Pi} \stackrel{\text{def}}{=} J \underline{\sigma} \cdot \underline{F}^{-T}.$$

Then, the principle of virtual work becomes

$$\forall \underline{v} \in \mathcal{V}, \int_{\Gamma_{0N}} \rho_0 \underline{\gamma} \cdot \underline{v} \, d\Omega + \int_{\Gamma_{0N}} \underline{\Pi} : \underline{\nabla}_{\underline{\xi}} \underline{v} \, d\Omega$$

$$= \int_{\Gamma_{0N}} \rho_0 \underline{f} \cdot \underline{v} \, d\Omega + \int_{\partial\Gamma_{0N}} \underline{t}_0 \cdot \underline{v} \, dS, \tag{3}$$

where

$$\underline{t}_0 = J \underline{\Pi} \underline{F}^{-T} \cdot \underline{n}_0 \underline{\underline{t}},$$

which gives a strong formulation comparable to (1), namely

$$\rho_0 \underline{\gamma} - \text{div}_{\underline{\xi}} \underline{\Pi} = \rho_0 \underline{f}_0, \text{ in } \Omega_0. \tag{4}$$

We recall that we can also express the variational formulation (4) using symmetric stress and strain tensors “symmetrizing” the deformation gradient in the reference configuration. In that case, we classically introduce the second Piola–Kirchhoff stress tensor

$$\underline{\Sigma} \stackrel{\text{def}}{=} J \underline{F}^{-1} \cdot \underline{\sigma} \cdot \underline{F}^{-T},$$

and the Green–Lagrange strain tensor  $\underline{e}$

$$\underline{e} = \frac{1}{2} \left( \underline{\nabla}_{\underline{\xi}} \underline{y}_s + \underline{\nabla}_{\underline{\xi}} \underline{y}_s^T + \underline{\nabla}_{\underline{\xi}} \underline{y}_s \cdot \underline{\nabla}_{\underline{\xi}} \underline{y}_s^T \right),$$

which satisfies

$$d_y \underline{e} \cdot \underline{v} = \frac{1}{2} \left( (d_y \underline{F} \cdot \underline{v})^T \cdot \underline{F} + \underline{F}^T \cdot d_y \underline{F} \cdot \underline{v} \right).$$

Hence, the variational formulation is

$$\forall \underline{v} \in \mathcal{V}, \int_{\Gamma_{0N}} \rho_0 \underline{\gamma} \cdot \underline{v} \, d\Omega + \int_{\Gamma_{0N}} \underline{\Sigma} : d_y \underline{e} \cdot \underline{v} \, d\Omega$$

$$= \int_{\Gamma_{0N}} \rho_0 \underline{f} \cdot \underline{v} \, d\Omega + \int_{\partial\Gamma_{0N}} \underline{t}_0 \cdot \underline{v} \, dS, \tag{5}$$

and we will see the advantages of such formulations when defining the constitutive law characterizing the materials.

When assuming small displacements,  $\Omega(t)$  and  $\Omega_0$  are considered identical. Hence, all formulations can be written using the Cauchy stress tensor  $\underline{\sigma}$  and the linearized strain tensor  $\underline{\varepsilon}$  in the reference configuration  $\Omega_0$ .

### 3.1.3 Constitutive laws and fluid–structure interaction

The previous section introduced the required classical notations for solid or fluid mechanical systems. We now have to particularize the behavior in each domain. We will systematize the use of indices  $f$  or  $s$  to denote quantities attached to the fluid or solid subsystems, respectively. For instance, the Cauchy stress tensors are respectively denoted by  $\underline{\underline{\sigma}}_f$  in the fluid and by  $\underline{\underline{\sigma}}_s$  in the solid.

First considering the fluid, we assume the behavior to be incompressible and Newtonian, therefore

$$\underline{\underline{\sigma}}_f(\underline{u}_f, p_f) \stackrel{\text{def}}{=} -p_f \underline{\underline{1}} + 2\mu_f \underline{\underline{\varepsilon}}(\underline{u}_f),$$

where  $p_f$  denotes the pressure and  $\mu_f$  the dynamic viscosity. Note that fluid formulations are generally written in the deformed configuration, namely in a Eulerian framework.

Concerning the solid formulation—generally written in the reference configuration—we assume we have an isotropic elastic behavior that we may treat as a hyperelastic material with added viscous stresses simply modeled as proportional to the strain rate, namely

$$\underline{\underline{\Sigma}} \stackrel{\text{def}}{=} \frac{\partial W_s}{\partial \underline{\underline{\varepsilon}}} + \eta_s \underline{\underline{\dot{\varepsilon}}}, \quad (6)$$

with  $W_s$  the hyperelastic potential—see Sect. 3.3.1. Upon linearization with respect to displacement and velocity—namely within the small displacement assumption—this law reduces to

$$\underline{\underline{\sigma}}_s(\underline{y}_s) = \underline{\underline{\Sigma}}_0 + \lambda_s \text{Tr}(\underline{\underline{\varepsilon}}(\underline{y}_s)) \underline{\underline{1}} + 2\mu_s \underline{\underline{\varepsilon}}(\underline{y}_s) + \eta_s \underline{\underline{\varepsilon}}(\underline{u}_s), \quad (7)$$

with  $\underline{\underline{\Sigma}}_0$  the prestress and  $\lambda_s$  and  $\mu_s$  the Lamé constants. Nearly incompressible formulations are obtained by considering a large bulk coefficient in the hyperelastic potential or a large  $\lambda_s$  in (7).

The fluid and solid formulations are then coupled through the transmission conditions

$$\underline{u}_f = \underline{u}_s, \quad \underline{\underline{\sigma}}_f \cdot \underline{n}_f + \underline{\underline{\sigma}}_s \cdot \underline{n}_s = 0, \quad \text{on } \Sigma, \quad (8)$$

where  $\underline{n}_f$  and  $\underline{n}_s$  respectively denote the outward unit normal vectors on  $\partial\Omega^f$  and  $\partial\Omega^s$ .

## 3.2 Cardiovascular modeling

### 3.2.1 Blood flow domain boundary conditions

We introduce some notation for the blood flow domain  $\Omega^f(t)$  (see Fig. 1), for which the boundary decomposes into

$$\partial\Omega^f(t) = \Gamma_{\text{in}}^f(t) \cup \Sigma(t) \cup \Gamma_{\text{out}}^f(t);$$

where  $\Gamma_{\text{in}}^f(t)$  represents an inflow face of the model—the aortic root in our case—on which a velocity field  $\underline{u}_f = \underline{u}_f^{\text{in}}$

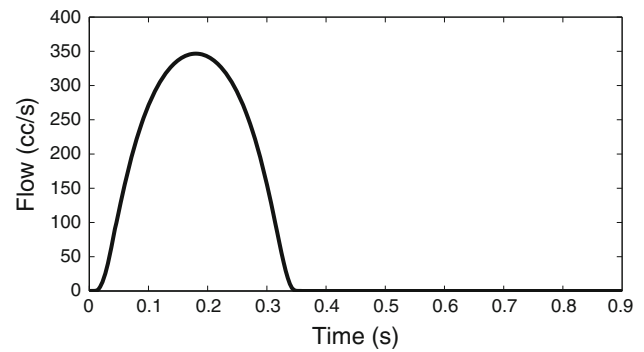


**Fig. 3** Volumetric flow waveform used to prescribe a flat velocity profile at the inlet face  $\Gamma_{\text{in}}^f(t)$

is prescribed. By contrast,  $\Gamma_{\text{out}}^f(t)$  is an outflow face of the model where a traction field  $\underline{t}_{\text{out}}$  is weakly prescribed. In our case,  $\Gamma_{\text{out}}^f(t)$  is divided into four parts:

$$\Gamma_{\text{out}}^f(t) = \bigcup_{1 \leq i \leq 4} \Gamma_{\text{out}}^{f,(i)}(t)$$

with the brachiocephalic artery ( $i=1$ ), left common carotid artery (2), left subclavian artery (3), and distal part of the thoracic aorta (4).

*Inflow condition at the aortic root face.* In this work, we considered an idealized volumetric waveform (see Fig. 3) mapped to a flat velocity profile  $\underline{u}_f^{\text{in}}$  on the aortic root face  $\Gamma_{\text{in}}^f(t)$ . This waveform generates a typical cardiac output (5 liters/minute) and heart rate (67 beats per minute) for an adult man. The waveform shape is representative of aortic root flow, with a systolic phase spanning over one-third of the cardiac cycle and with no flow during diastole, following the closure of the aortic valve.

*Models for the downstream vasculature.* In this paper, we used a “coupled-multidomain” approach whereby the solution at the outflow boundaries of the “upstream” FSI domain is coupled to a reduced-order model (i.e., one-dimensional or zero-dimensional) of the “downstream” domain (Vignon-Clementel et al. 2006). This reduced-order model may be an impedance function relating modes of flow and pressure in the distal arterial tree, a nonlinear finite element solution of the one-dimensional equations of blood flow, or a lumped-parameter model of the distal circulation. In this approach, a traction  $\underline{t}_{\text{out}}$  related to the pressure field in the “downstream” domain is prescribed weakly as a boundary condition for the “upstream” FSI domain. Here, we used a Windkessel model that represents a convenient alternative for outflow boundary condition specification due to its ability to accommodate transient phenomena in the “upstream” FSI domain (Vignon-Clementel et al. 2010). More precisely, we considered a 3-element Windkessel model coupled at each outlet  $\Gamma_{\text{out}}^{f,(i)}(t)$  as sketched in Fig. 1. In this model, the ratio of the

proximal resistance  $R_p$  to the distal resistance  $R_d$  regulates the amount of backflow, whereas the capacitance  $C$  is related to the pressure pulse (i.e. difference between diastolic and systolic pressure) at the outlet. The associated Windkessel pressure satisfies the differential equation

$$\begin{cases} C \dot{P}_i^w + \frac{1}{R_d} P_i^w - \int_{\Gamma_{\text{out}}^{f,(i)}(t)} \underline{u}_f \cdot \underline{n}_{\text{out}}^{(i)} dS = 0, \\ R_p \int_{\Gamma_{\text{out}}^{(i)}(t)} \underline{u}_f \cdot \underline{n}_{\text{out}}^{(i)} dS = \frac{1}{|\Gamma_{\text{out}}^{f,(i)}(t)|} \int_{\Gamma_{\text{out}}^{f,(i)}(t)} p_f dS - P_i^w \end{cases}$$

Then, considering the Neumann outflow boundary condition for the fluid, we get on each  $\Gamma_{\text{out}}^{f,(i)}(t)$ ,  $\underline{t}_{\text{out}} = -p_f \underline{n}_{\text{out}}^{(i)}$ . Hence, we have the following expression for the virtual work of the outflow conditions

$$\mathcal{P}_{\text{wind}}(\underline{v}) = - \sum_{1 \leq i \leq 4} \int_{\Gamma_{\text{out}}^{f,(i)}(t)} p_f \underline{n}_{\text{out}}^{(i)} \cdot \underline{v} dS.$$

Note that depending on the method used to solve the Navier–Stokes equations, it can be convenient—and physically justified indeed—to replace  $p_f$  by  $(\underline{\sigma}_f \cdot \underline{n}) \cdot \underline{n}$  in the above differential equation.

*Backflow situations.* A comment should be made regarding situations where complex or reverse flow structures develop at the outflow boundaries of the blood flow domain. Here, the weak traction condition coupled to a reduced-order model of the distal vasculature usually results in diverging simulations. A common but rather rudimentary workaround to this problem has consisted of artificially extending the outflow branches using long straight segments to regularize the flow. Recently, new formulations have been developed to resolve this issue numerically. Formaggia et al. (2007) implemented a total pressure boundary condition by constructing a special formulation of the Navier–Stokes equations. Kim et al. (2009) have proposed an augmented Lagrangian formulation for constraining the shape of velocity profiles at inlet and outlet boundaries, rendering stable solutions regardless of the complexity of the blood flow.

*Parametrization and calibration.* The parameters of the Windkessel model for each outlet  $\Gamma_{\text{out}}^{f,(i)}(t)$  can be tuned to match any given flow distribution and systolic and diastolic pressure data. This process may be cumbersome (Les et al. 2010), due to the lack of sufficient data to uniquely define all the parameters of the Windkessel model. This task may be automated using data assimilation or optimization procedures (Moireau et al. 2008; Spilker and Taylor 2010). This also relates to the already-discussed importance of adequate time registration of geometric (i.e., image data) and boundary condition (i.e., blood flow and blood pressure) in order to avoid the appearance of non-physiologic, spurious motion modes in the FSI simulation.

### 3.2.2 Vessel wall domain boundary conditions

Once the blood flow boundary conditions are specified, we must determine the vessel wall boundary conditions with the same care. Here, we refer to boundary conditions in the widest sense: all the modeling elements applied to the bounds of the vessel wall domain, namely the exterior walls, the aortic root, and the distal section of the descending aorta. On these boundaries, we will use an extended Robin condition as illustrated in Fig. 1 to represent a simplified but robust model of the mechanical relations between the system of interest and the external tissues and organs, with natural physiological interpretations.

*External tissue support.* The influence of external tissues and organs tethering and constraining the movement of blood vessels is of critical importance when simulating fluid–structure interactions in the arterial system. In particular, the descending thoracic aorta is longitudinally tethered by the spine, whereas the ascending aorta is less constrained by external tissues and structures. Obviously, it is currently infeasible to model the detailed multicontact relations between the aortic system and the other tissues. Therefore, we have chosen to handle the external tissue support on the outer arterial wall by enforcing the following Robin boundary conditions:

$$\underline{\sigma}_s \cdot \underline{n}_s = -k_s \underline{y}_s - c_s \underline{u}_s - p_0 \underline{n}_s, \text{ on } \Gamma^s. \tag{9}$$

In general, the parameters  $k_s$ , and  $c_s$  depend on space, and possibly on time. They respectively model an elastic and a viscoelastic response of the external tissue. We point out that even if we do not use time-dependent parameters in this paper, they could be employed to model the effect of the change of mechanical properties in some tissues over time—for instance in the lungs during breathing. In addition,  $p_0$  represents the intrathoracic pressure that can also be considered as varying in space and time, in particular due to breathing effects. Since the image data considered in this paper was acquired under breath-hold conditions, we will neglect time-varying effects.

From a variational standpoint, this Robin boundary condition is easy to implement since it corresponds to the straightforward virtual work

$$\begin{aligned} \forall \underline{v} \in \mathcal{V}, \quad \mathcal{P}_{\text{support}}(\underline{v}) \\ = - \int_{\Gamma^s} (k_s \underline{y}_s \cdot \underline{v} + c_s \underline{u}_s \cdot \underline{v} + p_0 \underline{n}_s \cdot \underline{v}) dS. \end{aligned}$$

*Heart motion modeling.* Except for certain aortic pathologies, the large displacements of the ascending aorta are heavily influenced by the heart motion. Here, modeling the entire heart system would necessitate a modeling effort as complex as for the problem at hand, i.e. fluid–structure interactions

in the thoracic aorta. Therefore, we represent the heart influence by a similar Robin boundary condition, but here with a forcing term

$$\underline{\sigma}_s \cdot \underline{n}_s = -k_s(\underline{y}_s - \underline{y}_b), \text{ on } \Gamma_{\text{in}}^s, \quad (10)$$

where  $\underline{y}_b$  is a prescribed displacement that can be extracted from the image data. Indeed, the approximately rigid body motion that the heart induces on the aortic root can be detected by observing the region near the sinuses of Valsalva. In order to extract this rigid motion, we track the sinotubular junction and obtain the translation of its barycenter and the rotation of its normal axis. We then obtain the rotation around the normal axis by tracking the sinuses of Valsalva themselves. This rigid motion can then be applied to the sinotubular boundary section of our domain using any well-chosen time interpolation, such as linear or Fourier interpolation between two consecutive image frames.

Here, we emphasize that we do not apply the extracted displacement  $\underline{y}_b$  directly as a Dirichlet condition because the heart motion is more complex than a simple rigid motion and in particular we want to allow the aorta to dilate radially in the vicinity of the inlet section. Furthermore, a strong enforcement of a displacement field from a relatively noisy image data would also be inadequate. Practically speaking, it means that the coefficient  $k_s$  should not be chosen too large.

We should also point out that the vessel wall inlet boundary condition must be compatible with the blood flow domain inlet boundary condition. In this respect, we recall that the inflow waveform constructed from physiological considerations (see Fig. 3) and according to the ejection fraction of the specific patient considered is always a *relative* flow and that is therefore added to the fluid domain velocity at the inlet.

Finally, we can also include a viscoelastic contribution in the heart motion model such that

$$\underline{\sigma}_s \cdot \underline{n}_s = -k_s(\underline{y}_s - \underline{y}_b) - c_s(\underline{u}_s - \underline{u}_b), \text{ on } \Gamma_{\text{in}}^s,$$

where  $\underline{u}_b$  is the derivative in time of  $\underline{y}_b$ . However, if  $\underline{u}_b$  is not directly measured, numerical differentiation of the noisy signal  $\underline{y}_b$  may render a poor estimate of the velocity field  $\underline{u}_b$ .

*Distal vessel mechanical modeling.* The Robin boundary condition (9) is also utilized on the solid outlets  $\Gamma_{\text{out}}^{s,(i)}$ ,  $1 \leq i \leq 4$ , where imposing classical homogeneous Dirichlet conditions presents a major drawback: non-physiological reflections and high frequency vibrations may occur as a consequence of attaching the system at the outlets. Here, the vessel wall is tethered by the external tissue support and we can therefore relax the Dirichlet condition.

*Parametrization and calibration.* A difficulty of the simplified representation of the external tissue (9) is the determination of the phenomenological parameters  $k_s$  and  $c_s$ . These parameters can be tuned to ensure that the simulation matches

the image data typically by subdividing the boundary concerned into physiologically based regions within which these parameters can be assumed to be e.g. constant or linearly varying. Note that in essence by calibrating just these few parameters representing the boundary support, we regularize the corresponding displacements, as opposed to directly extracting displacements from the noisy image sequence. Furthermore, this task can be automated *via* a data assimilation procedure inspired from Moireau et al. (2009), Moireau and Chapelle (2010) and already applied in fluid–structure interaction problems (Bertoglio et al. 2009) that will be presented in a forthcoming work. Of course, the predictivity of our model must then be assessed according to the reproducibility of the approach for various patients in several hemodynamic states, see the results section for two cases, to be confirmed for more subjects in future studies.

### 3.2.3 Initial configuration

We have used the diastolic phase of the cardiac-gated CT data to generate the initial blood flow domain mesh. For the ALE FSI model, we generated the vessel wall domain by extrusion of the boundary  $\Sigma$ . The blood flow domain is initialized by calculating the steady solution of a rigid wall Navier–Stokes flow with a prescribed input flow corresponding to the average cardiac output—namely the stroke volume multiplied by the heart rate. On the structure side, however, one major difficulty lies in that the configuration coming from the segmentation corresponds to a loaded state with a typical arterial pressure of 80 mmHg. The problem is thus to obtain the load-free  $\Omega_0$  configuration corresponding to the loaded configuration  $\Omega(t_0)$ . The strategy to define this load-free configuration depends on the kinematic assumption made for the structure: small or large displacements.

*Large displacements.* In order to compute the mapping from the (unknown) reference load-free configuration onto the initial loaded configuration, we use the residual  $\mathcal{P}_{\Sigma(t_0)}^f$  obtained from the rigid wall fluid solution on the interface. We then solve the following inverse problem:

Find  $\underline{\phi}_s$  and  $\Omega_0 = \underline{\phi}_s^{-1}(\Omega^s(t_0))$  such that

$$\forall \underline{v} \in \mathcal{V}, \quad \int_{\Omega_0} \underline{\Sigma} : \underline{d}_{\underline{y}} \underline{e} \cdot \underline{v} \, d\Omega = \mathcal{P}_{\Sigma(t_0)}^f(\underline{v}). \quad (11)$$

In practice, we solve this inverse problem using a simple fixed point algorithm. Given a tentative reference configuration  $\Omega_0^{(k)}$ , we compute the displacements associated with the residual and update the configuration into  $\Omega_0^{(k+1)}$  by using the discrepancy between the computed deformed configuration  $\underline{\phi}_s^{(k)}(\Omega_0^{(k)})$  and  $\Omega(t_0)$ , using an adequate relaxation parameter. This approach is therefore very similar to the first method presented in Gee et al. (2010).

*Small displacements.* In this case, the computational domain does not change in time and the problem is linear with respect to the loading. Therefore, the residual  $\mathcal{P}_{\Sigma(t_0)}^f$  can be seen in (11) as the result of a *prestress* on the structure. We thus solve the linear problem with this prestress contribution  $\underline{\underline{\Sigma}}^{ps}$  added to  $\underline{\underline{\Sigma}}_0$  in (7).

### 3.3 Models formulation

#### 3.3.1 First model: ALE formulation

We adopt an Arbitrary Lagrangian–Eulerian (ALE) formulation in the fluid by introducing another mapping,

$$\phi_{\mathcal{A}} : \Omega_0^f \times [0, T] \longrightarrow \Omega^f(t),$$

such that  $\phi_{\mathcal{A}}|_{\Sigma_0} = \phi_s|_{\Sigma_0}$ , which in general does not follow the material trajectories inside the domain. We then introduce the corresponding deformation gradient  $\underline{\underline{F}}_f(\underline{\xi}, t) = \underline{\underline{\nabla}}_{\underline{\xi}} \phi_{\mathcal{A}}(\underline{\xi}, t)$ , and determinant  $J_f(\underline{\xi}, t) = \det \underline{\underline{F}}_f(\underline{\xi}, t)$ . The fluid domain velocity is denoted by  $\underline{w}(\underline{\xi}, t) = \partial_t \phi_{\mathcal{A}}(\underline{\xi}, t)$ . Note that we then have  $\underline{w}|_{\Sigma_0} = \underline{u}_s|_{\Sigma_0}$ , hence we have thus defined an extension map such that

$$\underline{w} = \text{Ext}(\underline{u}_s|_{\Sigma_0}), \quad \text{in } \Omega_0^f.$$

The strong form of the coupled fluid–structure problem reads:

$$\begin{cases} \underline{w} = \text{Ext}(\underline{u}_s|_{\Sigma_0}), & \text{in } \Omega_0^f, \\ \left. \begin{aligned} \frac{\rho_f}{J_f} \frac{\partial J_f \underline{u}_f}{\partial t} \Big|_{\underline{\xi}} + \rho_f (\underline{u}_f - \underline{w}) \cdot \underline{\underline{\nabla}}_{\underline{x}} \underline{u}_f \\ - 2\mu \text{div}_{\underline{x}} (\underline{\underline{\varepsilon}}(\underline{u}_f)) + \underline{\underline{\nabla}}_{\underline{x}} p_f = \rho_f \underline{f}_f, \\ \text{div}_{\underline{x}} \underline{u}_f = 0, \end{aligned} \right\} & \text{in } \Omega^f(t), \end{cases} \quad (12)$$

$$\begin{cases} \rho_s \frac{\partial \underline{u}_s}{\partial t} - \text{div}_{\underline{\xi}} (\underline{\underline{\Pi}}) = 0, & \text{in } \Omega_0^s, \\ \underline{\underline{\sigma}}_s \cdot \underline{n}_s = -k_s (\underline{y}_s - \underline{y}_b), & \text{on } \Gamma_{\text{in}}^s, \\ \underline{\underline{\sigma}}_s \cdot \underline{n}_s = -k_s \underline{y}_s - c_s \underline{u}_s, & \text{on } \Gamma_s, \end{cases} \quad (13)$$

$$\begin{cases} \underline{u}_f = \underline{u}_s, & \text{on } \Sigma(t), \\ \underline{\underline{\Pi}} \cdot \underline{n}_s = J_f \underline{\underline{\sigma}}_f(\underline{u}_f, p_f) \cdot (\underline{\underline{F}}^f)^{-T} \cdot \underline{n}_s, & \text{on } \Sigma_0, \end{cases} \quad (14)$$

where  $\frac{\partial}{\partial t} \Big|_{\underline{\xi}}$  represents the ALE time derivative (see [Fernández and Gerbeau 2009](#) and references therein) and  $\underline{f}_f$  is a force per unit mass—for example the gravity that may not be negligible in the blood flow domain for long vertical arteries. For this coupled problem, we then include the boundary conditions prescribed on the fluid and structure problems as described in Sect. 3.2.

The weak formulation of this model can be written using three test function spaces  $\mathcal{V}^f, \mathcal{V}^s, \mathcal{Q}$ :

$$\begin{aligned} \forall t \in [0, T], \quad \forall \underline{v}_s \in \mathcal{V}^s, \quad \forall \underline{v}_f \in \mathcal{V}^f, \quad \forall q \in \mathcal{Q}, \\ \int_{\Omega^f(t)} \left( \left( \frac{\rho_f}{J_f} \frac{\partial J_f \underline{u}_f}{\partial t} \Big|_{\underline{\xi}} + \rho_f (\underline{u}_f - \underline{w}) \cdot \underline{\underline{\nabla}}_{\underline{x}} \underline{u}_f \right) \cdot \underline{v}_f \right. \\ \left. - p_f \text{div}_{\underline{v}_f} + 2\mu \underline{\underline{\varepsilon}}(\underline{u}_f) : \underline{\underline{\varepsilon}}(\underline{v}_f) + q \text{div}_{\underline{u}_f} \right) d\Omega \\ + \int_{\Omega_0^s} \left( \rho_s \frac{\partial \underline{u}_s}{\partial t} \cdot \underline{v}_s + \underline{\underline{\Sigma}} : \underline{d}_{\underline{y}_e} \cdot \underline{v}_s \right) d\Omega \\ = \int_{\Omega^f(t)} \rho_f \underline{f}_f \cdot \underline{v}_f d\Omega + \mathcal{P}_{\text{wind}}(\underline{v}_f) + \mathcal{P}_{\text{support}}(\underline{v}_s). \end{aligned} \quad (15)$$

We point out that in this formulation, the test functions in  $\mathcal{V}^f$  and  $\mathcal{V}^s$  are assumed to be compatible on the interface  $\Sigma$ .

Concerning the choice of constitutive law in the solid viscoelastic behavior, we use the hyperelastic potential given by the Ciarlet–Geymonat volumic energy ([Ciarlet 1988](#); [Le Tallec 1994](#))

$$W_s = \kappa_1(J_1 - 3) + \kappa_2(J_2 - 3) + \kappa(J - 1) - \kappa \ln J,$$

where  $J_1, J_2$ , and  $J$  denote the reduced invariants of the Cauchy–Green strain tensor  $\underline{\underline{C}} = \underline{\underline{F}}_s^T \cdot \underline{\underline{F}}_s$ . The last part of this potential is designed to penalize the incompressibility constraint when using large values for the bulk coefficient  $\kappa$ . We could use more sophisticated constitutive laws developed for arterial walls—for example with exponential terms and anisotropic strain energy functions, see e.g. [Fung \(1993\)](#), [Humphrey \(2003\)](#), [Holzapfel \(2006\)](#) and references therein—but we found the above choice to give satisfactory results in the range of deformations considered with respect to the initial loaded configuration, namely typically less than 10%. Note that changing the constitutive law would have an effect on the inferred stress-free configuration, which is unavailable in the data.

The spatial discretization of this formulation is performed using  $\mathbb{P}_1$ -Lagrange finite elements, well adapted to automatic mesh generation obtained from the segmented images. Concerning the fluid discretization, we use a Chorin–Temam projection scheme to handle the incompressibility constraint. The subiterations with the solid are only performed when solving the second step of this algorithm, namely the pressure computation (i.e. the velocity projection). This effective scheme was proposed in [Fernández et al. \(2006, 2007\)](#) and proven to be stable in energy norm under conditions that are typically satisfied in practice. We use a mid-point Newmark scheme for the solid, which is also stable for nonlinear visco-hyperelastic formulations with adequate choice of discretization for Piola–Kirchhoff tensors, see a comprehensive study in [Hauret and Le Tallec \(2006\)](#).

### 3.3.2 Second model: coupled momentum method

The coupled momentum method is based on a stabilized finite element formulation (Taylor et al. 1998; Whiting and Jansen 2001) of the equations for an incompressible Newtonian fluid discretized on a fixed computational grid. The method formulates the degrees of freedom (i.e., displacements  $\underline{y}_s$ ) for the vascular wall as a function of the fluid velocities  $\underline{u}_f$  at the fluid–solid interface using an “enhanced” linear membrane formulation. We assume that wall displacements are small so that the current configuration can be approximated by the reference configuration, and we define  $\Omega = \Omega^s \cup \Omega^f \stackrel{\text{def}}{=} \Omega_t = \Omega_0$ .

Considering the wall to be a thin membrane of given thickness  $h$ , we define the vessel wall problem in the domain  $\Omega^s = \Sigma \times h$  and we use the linear elastic model presented in Figueroa et al. (2006). This leads to a membrane stress tensor  $\underline{\underline{\sigma}}_m$  in which the twice-normal component is assumed to vanish. The boundaries of  $\Omega^s$  include  $\Gamma_{\text{in}}^s$  and  $\Gamma_{\text{out}}^s$  with a velocity prescribed on the former and a traction  $\underline{t}_s$  prescribed on the latter. The external tissue viscoelastic support conditions proposed in this article correspond to a distributed force

$$\underline{f}_{\text{support}} = -k_s \underline{y}_s - c_s \underline{u}_s$$

applied on the membrane surface—where  $k_s$  and  $c_s$  vanish outside a given area  $\Gamma_s \subset \Sigma$ .

The fluid–structure problem defined only on the fluid Eulerian configuration then reads

$$\begin{cases} \rho_f \frac{\partial \underline{u}_f}{\partial t} + \rho_f \underline{u}_f \cdot \underline{\nabla}_{\underline{x}} \underline{u}_f \\ -2\mu \text{div}(\underline{\underline{\varepsilon}}(\underline{u}_f)) + \underline{\nabla} p_f = \rho_f \underline{f}_f, & \text{in } \Omega^f, \\ \text{div} \underline{u}_f = 0, & \text{in } \Omega^f, \\ \underline{u}_f = \underline{u}_s, & \text{on } \Sigma, \end{cases} \quad (16)$$

$$\begin{cases} \rho_s \frac{\partial \underline{u}_s}{\partial t} - \text{div} \underline{\underline{\sigma}}_m = \frac{1}{h} \underline{f}_{\text{support}}, & \text{in } \Sigma \times h, \\ \underline{\underline{\sigma}}_m \cdot \underline{n}_s = \underline{\underline{\sigma}}_f(\underline{u}_f, p) \cdot \underline{n}_s, & \text{on } \Sigma. \end{cases} \quad (17)$$

This strong form after a proper choice of trial and weighting functional spaces can produce the following global variational equation for the coupled momentum method

$$\begin{aligned} \forall t \in [0, T], \quad \forall \underline{v} \in \mathcal{V}, \quad \forall q \in \mathcal{Q}, \\ \int_{\Omega^f} \left( \left( \rho_f \frac{\partial \underline{u}_f}{\partial t} + \rho_f \underline{u}_f \cdot \underline{\nabla}_{\underline{x}} \underline{u}_f \right) \cdot \underline{v} \right. \\ \left. - p_f \text{div} \underline{v} + 2\mu \underline{\underline{\varepsilon}}(\underline{u}_f) : \underline{\underline{\varepsilon}}(\underline{v}) + q \text{div} \underline{u}_f \right) d\Omega \\ + \int_{\Sigma} h \left( \rho_s \frac{\partial \underline{u}_s}{\partial t} \cdot \underline{v} + \underline{\underline{\sigma}}_m : \underline{\underline{\nabla}} \underline{v} \right) dS + \text{stabilization terms} \\ = \int_{\Omega^f} \rho_f \underline{f}_f \cdot \underline{v} d\Omega + \mathcal{P}_{\text{wind}}(\underline{v}) + \mathcal{P}_{\text{support}}(\underline{v}), \end{aligned} \quad (18)$$

where  $\mathcal{P}_{\text{support}}$  contains the following surface- and line-distributed terms

$$\mathcal{P}_{\text{support}}(\underline{v}) = \int_{\Sigma} \underline{f}_{\text{support}} \cdot \underline{v} dS + \int_{\Gamma_{\text{out}}^f} \underline{t}_s \cdot \underline{v} dL.$$

## 4 Results

### 4.1 First subject: 37-year-old man with large thoracic aorta motion

#### 4.1.1 Data processing

The data for this model problem was obtained from a thoracic CT angiographic scan of a 37-year-old subject. This subject presented significant thoracic aortic wall motion, a common circumstance for a relatively healthy and young individual. The FSI model of choice for this subject is the ALE formulation due to the large displacements experienced in the domain of interest. The extracted geometry includes the vascular lumen of the ascending and descending thoracic aorta as well as the major neck vessels, see Fig. 4.

From the segmentation, we generated a finite element mesh for the fluid domain of approximately 23.000 nodes and 110.000 tetrahedra. A vessel wall mesh of approximately 18.000 nodes and 24.000 tetrahedra was generated by extrusion of the lumen boundary  $\Sigma$ , using two layers of elements across the vessel wall thickness. The thickness was set to 1 mm near the outflow boundaries of the smaller arteries  $\Gamma_{\text{out}}^{(i)}$ ,  $1 \leq i \leq 3$  and to 2 mm on the aorta itself, having a gradual variation of thickness near the junctions. The external surface of the mesh is shown in Fig. 5. On the boundary of the solid mesh, we defined 6 regions used to prescribe the viscoelastic support boundary conditions with different parameter values (listed in Table 3). In particular, we identified a region adjacent to the spine by locating the intercostal artery attachments, as shown in Figs. 1 and 5. On any given cross-section of the descending aorta, we can therefore distinguish three different segments given by the region in contact with the spine, the spine vicinity and the region opposite to the spine.

In Fig. 6, we show the effect of the rigid body motion weakly prescribed on the inlet ring  $\Gamma_{\text{in}}^s$  as explained in Sect. 3.2.2, and we compare this displaced ring with the segmented aortic root processed from the ten phases of the cardiac-gated CT data. We can see that the inlet ring remains very close to the artery contour at all times of the cycle, despite the large displacements undergone by the aortic root—typically of the order of the vessel radius. This comparison validates the computation of the rigid motion of the inlet ring.

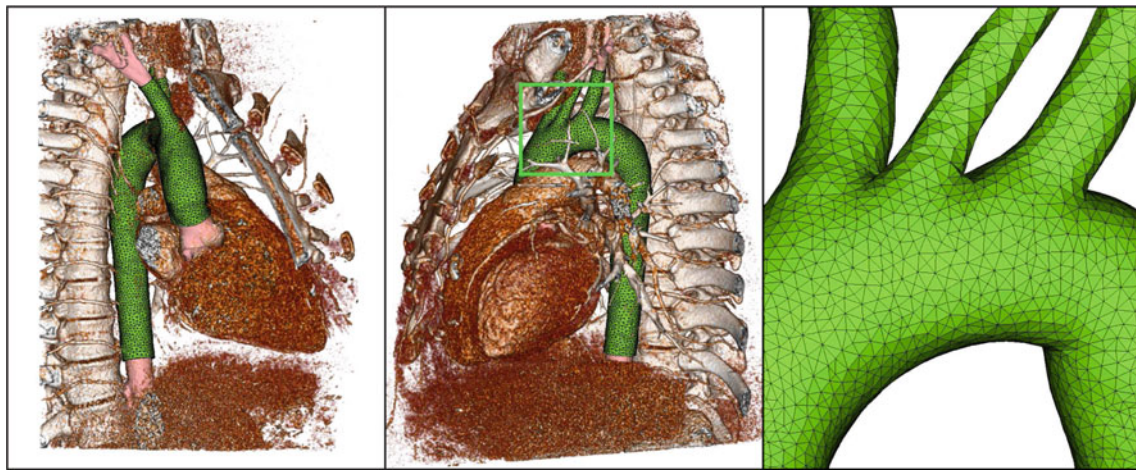


**Fig. 4** First subject: CT volume rendering, segmentation, and associated computational mesh

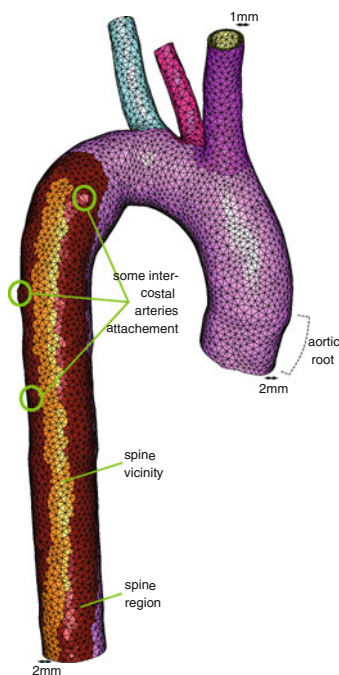


**Fig. 5** Initial solid mesh extruded from fluid mesh with defined regions. Loaded configuration and reference configuration for ALE simulation

#### 4.1.2 Simulation results

We start by solving the “loaded to reference configuration” inverse problem discussed in Sect. 3.2.3 in order to obtain a reference stress-free configuration. The corresponding mesh is shown in Fig. 5 and compared to the initial (loaded) configuration.

Using the inlet flow displayed in Fig. 3 and the material parameters given in Tables 1, 2 and 3, we computed several cardiac cycles of pulsatile blood flow and vessel wall motion with and without external tissue support. All the Windkessel

parameters (see Table 1) were calibrated in order to obtain physiologically relevant flow and pressure distributions and a periodic response, see Fig. 8. We point out that, in order to compensate for the absence of viscoelastic support, the internal viscosity parameter in the vessel wall ( $\eta$ ) was increased by a factor of 10 to obtain a stable behavior.

In order to assess the simulated motion, Fig. 8 shows 4 cross-sections of the calculated ALE model contours superimposed with the image data at peak systole and diastole. Figure 7 summarizes the error indicators obtained by computing distances between the model contours and the segmented walls in the above-described 6 separate regions, and using two different norms, namely the  $L^\infty$  and  $L^2$  norms.

#### 4.2 Second subject: 59-year-old man with small thoracic aorta motion

##### 4.2.1 Data processing

In contrast to the first clinical case, this case corresponds to a 59-year-old patient presenting a relatively small thoracic aortic wall motion, as is typical of older patients with stiffer arteries. This subject presented a slight aneurysmal dilation of the aortic root with maximal measurements of the sinus of Valsalva of 46 mm. Otherwise, the remainder of the thoracic aorta is normal in caliber. The FSI model of choice for this subject is the coupled momentum method due to the smaller displacements undergone in the domain of interest. As in the first subject, we used a thoracic cardiac-gated CT angiographic scan, and the extracted geometry includes the vascular lumen of the ascending and descending thoracic aorta as well as the major neck vessels, see Fig. 9.

From the segmentation, we generated a finite element mesh for the fluid domain of approximately 160.000 nodes and 800.000 tetrahedra. The thickness of the vessel wall was

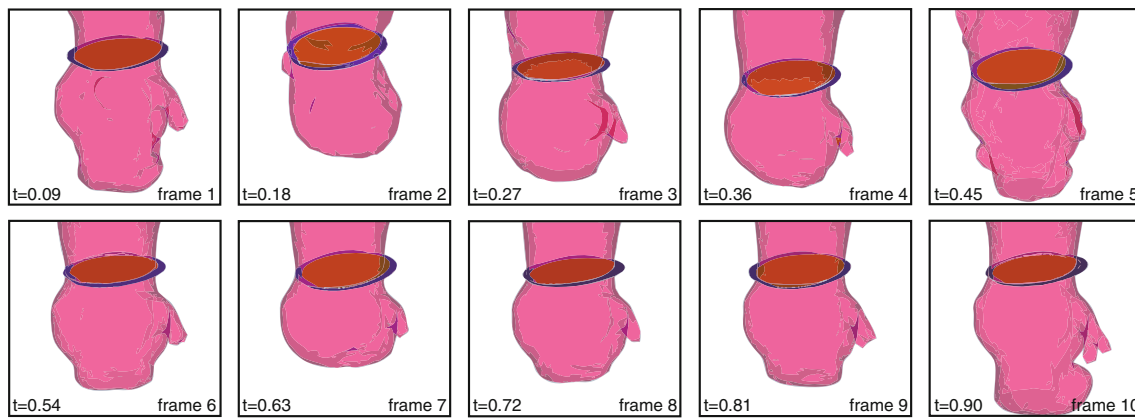


**Fig. 6** Rigid body motion prescribed on inlet ring of the computational mesh compared with the segmented wall along the cardiac cycle

**Table 1** Windkessel RCR parameters (units: cgs)

$\Gamma_{\text{out}}^{f,(i)}$	1	2	3	4
$R_p$	$0.05 \times 10^4$	$0.19 \times 10^4$	$0.075 \times 10^4$	$0.015 \times 10^4$
$R_d$	$0.85 \times 10^4$	$3.22 \times 10^4$	$1.25 \times 10^4$	$0.25 \times 10^4$
$C$	$0.95 \times 10^4$	$0.25 \times 10^4$	$0.64 \times 10^4$	$3.17 \times 10^4$

**Table 2** First subject: constitutive parameters (units: cgs)

$h\kappa_1$	$6.71 \times 10^5$
$h\kappa_2$	$6.71 \times 10^5$
$h\kappa$	$1.333 \times 10^8$
$hE_{\text{equivalent}}$	$0.8 \cdot 10^6$
$\nu_{\text{equivalent}}$	0.49
$\eta$	$0.012 (\kappa_1 + \kappa_2)$
$\rho_s$	1.2
$\rho_f$	1
$\nu$	0.06

**Table 3** First subject: external tissue support parameters (units: cgs)

Region	$\Gamma_{\text{in}}^s$	Spine	Spine vic.	Op. to Spine	$\Gamma_{\text{out}}^{s,4}$
$k_s$	$10^7$	$10^7$	$10^4$	$10^3$	$2 \times 10^6$
$c_s$	0	$10^4$	$10^4$	$10^4$	$10^4$

set to 2 mm uniformly. On the vessel wall boundary, we defined 3 regions used to prescribe the viscoelastic support boundary conditions with different parameter values (listed in Table 4). Again, we identified a region adjacent to the spine by locating the ostia of the intercostal arteries.

#### 4.2.2 Simulation results

Using the inflow waveform given in Fig. 3 and the Windkessel outflow boundary conditions parameters given in Table 1, we

computed several cardiac cycles of pulsatile blood flow and vessel wall motion. Here, we used the end-diastolic pressure as a reference to calculate a prestress for the linear membrane model of the coupled momentum method. The structural stiffness and Poisson ratio for this subject are listed in Table 5. Note that the calibration leads to a much higher stiffness modulus for this case as expected from the above description. Furthermore, incompressibility is exactly enforced here, namely  $\nu = 0.5$ .

Figure 11 displays 3 cross-sections of the calculated coupled momentum method contours in the presence and absence of the external tissue support boundary condition superimposed with the image data. Figure 10 displays the distances between the model wall boundary and the segmented wall boundary.

## 5 Discussion

The comparisons between the numerical simulations and the image data in Figs. 8 and 11 display a very significant improvement when using external tissue support, for almost all sections considered and regardless of the method used for FSI. This is further confirmed by the quantitative assessment of the distances between the models and the image data presented in Figs. 7 and 10 in the two norms considered. Of course, the distance is particularly reduced—and dramatically so, indeed—for the spine region, whereas the smallest improvement occurs on the opposite side to the spine. We observe that the error is more effectively reduced in the first case (healthy younger subject) in the upper branch vessels bifurcation region. A possible explanation for the enhanced effectiveness of the ALE model in the first case lies in the fact that the nonlinear solid model used for the wall provides some bending stiffness—absent from the membrane model used in the coupled momentum method—and can therefore account for smoother deformations. In the second case, we

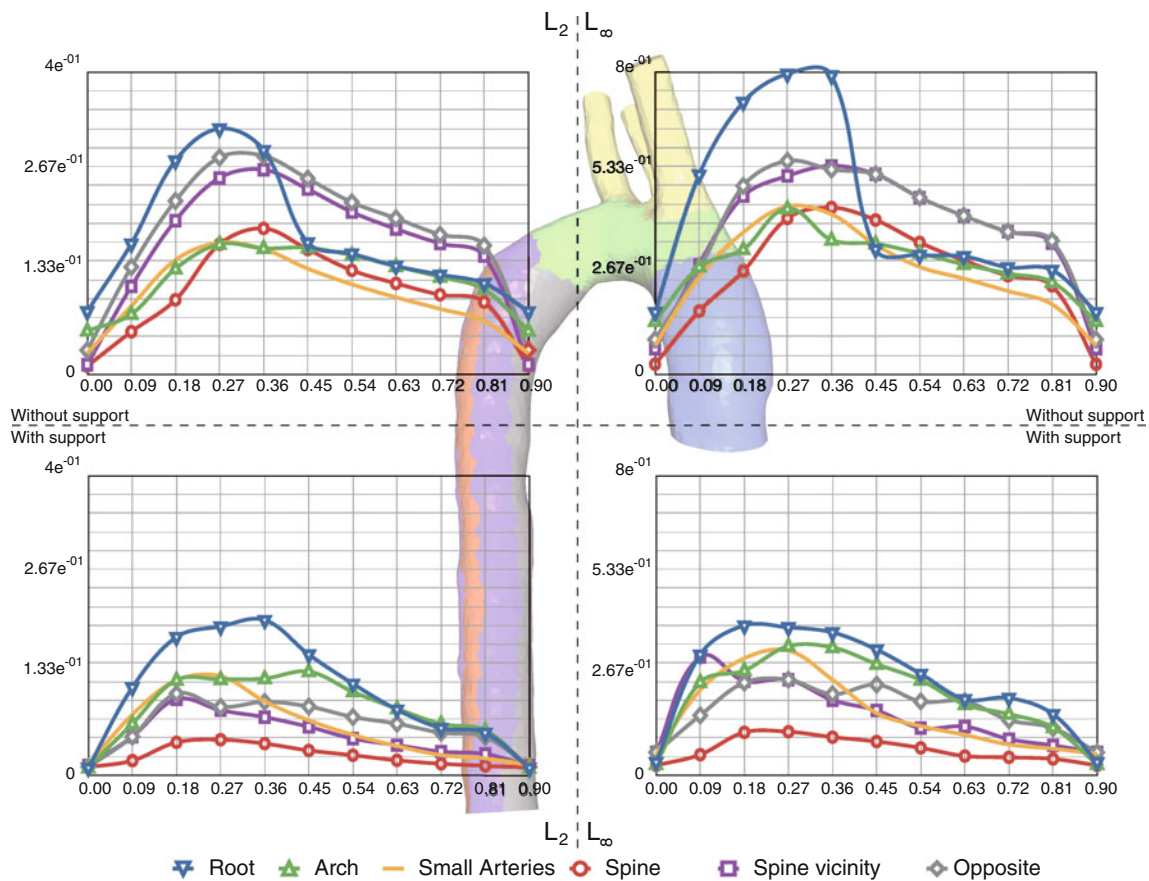


**Fig. 7** First subject:  $L^2$  and  $L^\infty$  (left and right resp.) norms of distances from the segmented wall boundary to the nodes of the model wall boundary using tissue support (bottom) and without tissue support (top). Distances versus time plots in cgs units (for comparison, vessel radius is approximately 2cm)

also observe that some rapid oscillations visible in the distances computed without tissue support are canceled when the external tissue support is considered – see in particular the distances in the spine region. This may be attributed to the presence of viscous dissipation in the support condition, whereas the membrane model used for the arterial wall itself is not dissipative. In addition, as expected, the errors in the second case are not significantly improved near the inlet, since there the fixed-grid model does not take into account the heart motion that is weakly prescribed in the first case, which also further validates the effectiveness of our heart motion forcing procedure. We emphasize, however, that imposing such large displacements necessitates an ALE formulation, which implies a substantial increase in the computational complexity.

Note further that all distances vary along the cardiac cycle and that in fact a maximum value of the distance is reached during systole even for the simulations with external tissue support. This could be expected, of course, as this is the stage corresponding to maximum amplitude in the actual vessel wall displacements, but should also be analyzed in light of the

linear expression used in the support condition (9). Indeed, this law roughly produces displacements proportional to the excitation, which is correlated to the amplitude of the actual displacements. Alternatively, we could consider other expressions for the support law, for instance derived from hyperelastic energies featuring exponential terms inspired by classical models of living tissue, see e.g. Fung (1993) and references therein. Such choices would more strongly penalize large displacements and would therefore reduce the larger errors observed in systole.

Nevertheless, the previous comparisons and error assessments clearly demonstrate the effectiveness and versatility of our approach to model external tissue boundary conditions corresponding to:

- both fixed and moving (with prescribed displacement) support;
- both natural and artificial boundaries, where by artificial we refer to boundaries corresponding to (inevitable) truncations of the geometry—namely the inlet and outlet here.

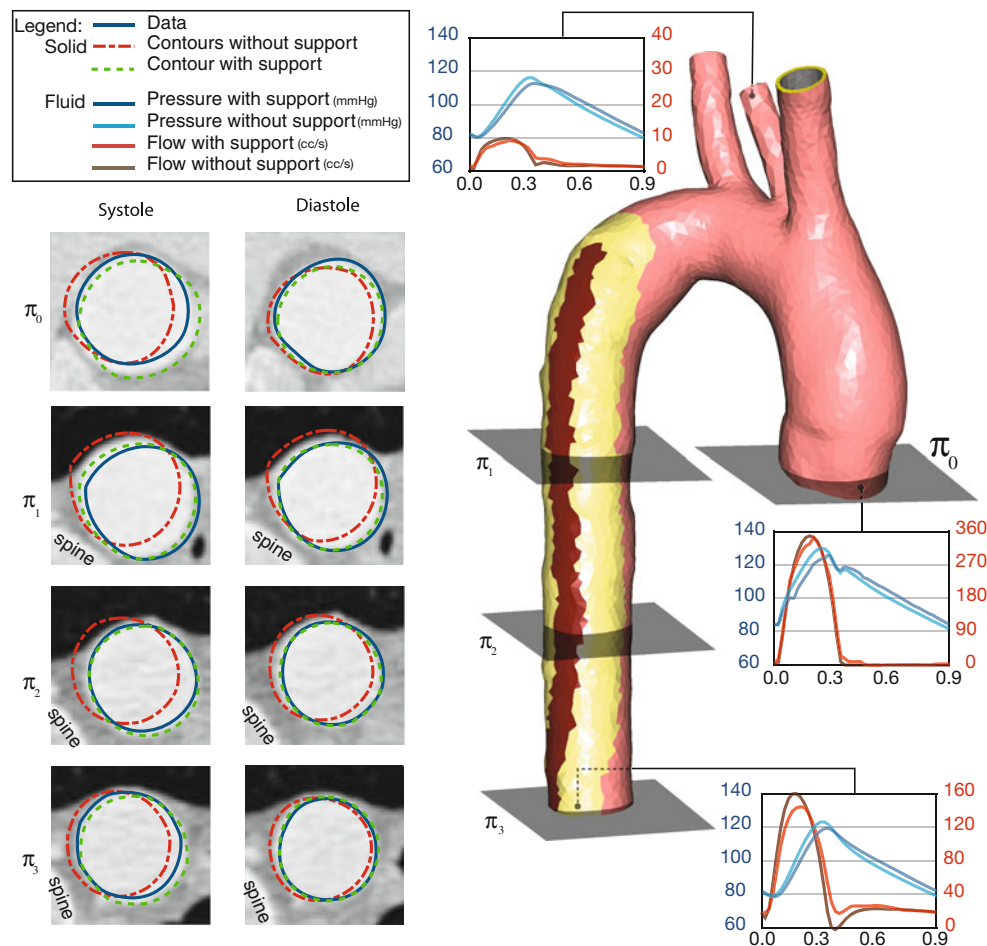


**Fig. 8** First subject: 2D contour comparison using external tissue support (*green contour*) and no external tissue support (*red contour*) at peak systole and diastole. The *solid blue contour line* represents the lumen boundary

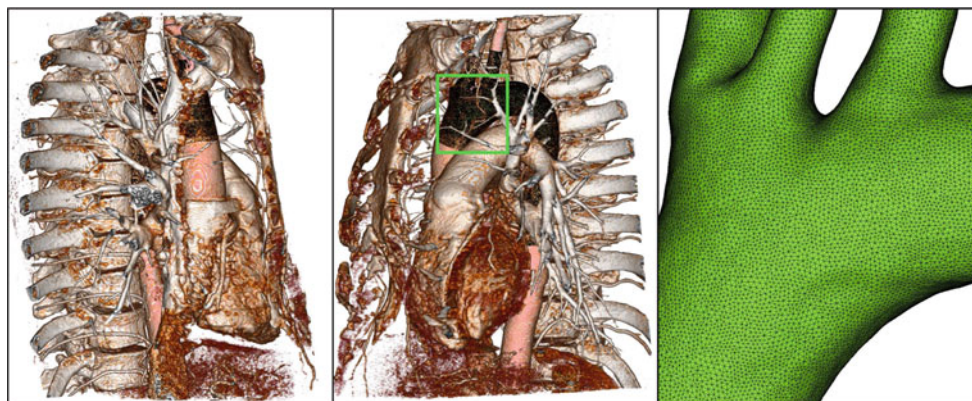


**Fig. 9** Second subject: CT volume rendering, segmentation, and associated computational mesh

Of course, the external tissue model presented here is simplified, both by construction as for all support conditions that account for the contribution of an infinite external medium and by the fact that the number of regions considered

for the support parameters is necessarily limited. In these regions, we have used piecewise-constant parameter values for calibration purposes. Note that, in order to facilitate parameter calibration, automatic estimation procedures

**Table 4** Second subject: external tissue support parameters (units: cgs)

Region	Spine	Spine vic.	Op. to Spine
$k_s$	$10^7$	$10^4$	$10^3$
$c_s$	$10^4$	$10^4$	$10^4$

**Table 5** Second subject: constitutive parameters (units: cgs)

$hE$	$2.8 \times 10^6$
$\nu$	0.50

can be considered as in Moireau et al. (2008), Moireau et al. (2009), Moireau and Chapelle (2010), Bertoglio et al. (2009). The estimation of these parameters is particularly interesting to obtain *personalized models* when inter-individual variability is present. For this procedure to be comprehensive, all other major uncertainties should then be estimated in addition to external tissue support parameters, in particular thickness and stiffness variabilities for the walls and Windkessel parameters for the outflow boundary conditions.

Note that, as regards the prescribed motion of the ascending aorta due to the action of the heart, we could also relax the rigid body kinematics by only enforcing conditions on the integrated displacements moments of order zero and one (i.e., global translations and global rotations, respectively), which would allow more freedom for the deformations of the inlet ring. Furthermore, an actual three-dimensional heart model could be considered for a more detailed kinematical prescrip-

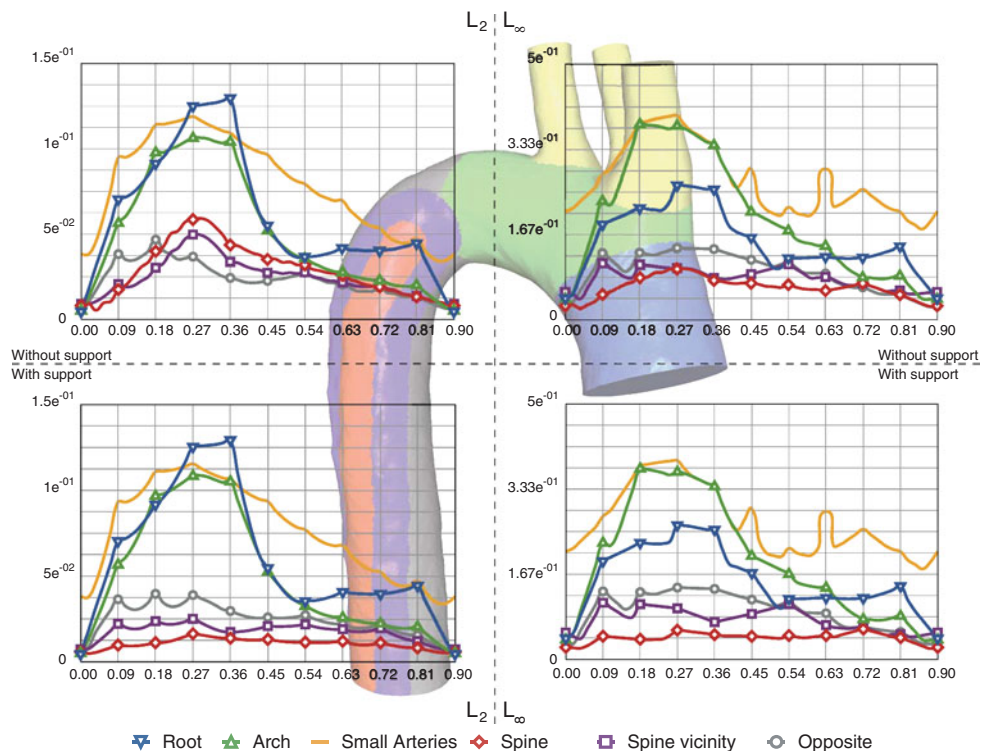
tion of the mechanics of the ascending thoracic aorta. In particular, the model presented and validated in Sainte-Marie et al. (2006), or a simplified—possibly reduced-order—version of this model with a sufficient number of modes (or degrees of freedom) to at least prescribe the required six rigid body components.

Finally, it is very clear that the constitutive laws used to model the arterial wall in our simulations are much simplified and that these laws should be substantially refined in order to capture some specific biomechanical phenomena. For example, the differential distribution of stresses across the vessel wall (Fung 1993; Alastrué et al. 2010) and the vasoactive component of smooth muscles included in the media layer (Humphrey 2003) could be considered. In this paper, our primary objective was to validate the external support model at a global level, and in this respect, we believe that our results substantiate the relevance of this modeling component *per se*, also in the perspective of considering different—more physiological—material laws. Of course, it should be kept in mind that calibrating such sophisticated material laws represents a significant challenge, especially with a view to patient-specific modeling.

### 6 Concluding remarks

In spite of the tremendous progress achieved in the recent years in the simulation of fluid–structure interaction in large

**Fig. 10** Second subject:  $L^2$  and  $L^\infty$  (left and right resp.) norms of distances from the segmented wall boundary to the nodes of the model wall boundary using tissue support (bottom) and without tissue support (top). Distances versus time plots in cgs units (for comparison, vessel radius is approximately 2cm)



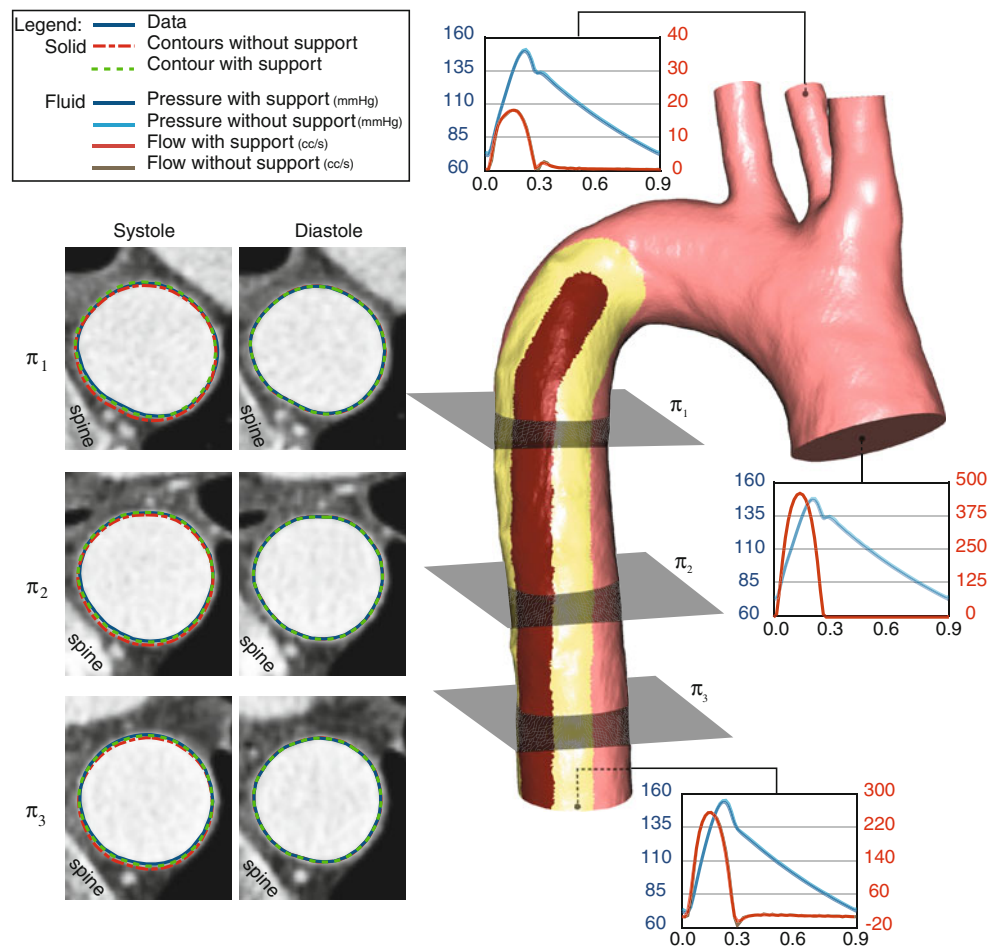


**Fig. 11** Second subject: 2D contour comparison using external tissue support (green contour) and no external tissue support (red contour) at peak systole and diastole. The solid blue contour line represents the lumen boundary

arteries, the modeling of the external tissue support has been rarely considered in the literature. The purpose of this paper was to propose a simple model that addresses this complex issue. To demonstrate its versatility, it has been implemented in two different fluid–structure interaction models. Although simple, the proposed approach has several benefits. From a biomechanical standpoint, it accommodates an improved description of the effect of surrounding tissues and organs of the thoracic cavity on the aorta. From a numerical standpoint, it improves the stability of complex FSI simulations. To roughly summarize its effect with respect to more conventional approaches, one could say that it constrains the motion in regions that are usually left free (i.e., the artery wall) and it relaxes some constraints in regions that are usually fixed (i.e., the inlet and the outlets). Moreover, the slight dissipation present in the model filters out the high frequencies, which is specially desirable when the structure model does not incorporate viscous effects.

This method has been illustrated with real patient anatomies and the wall displacements have been quantita-

tively assessed by detailed comparisons with corresponding dynamical sequences of medical images. In our simulation framework, multiple model parameters such as inflow, peripheral resistances and capacitances, and vessel wall constitutive parameters have been calibrated with care. However, this by no means represents a claim to genuine patient-specific modeling, which would necessitate a more systematic approach to accurately estimate the various parameter values, including spatially varying quantities (Bertoglio et al. 2009). This task was well beyond the scope of the present paper, but we intend to demonstrate the use of data assimilation procedures to estimate such parameters—among which those relating to the external tissue support—in future works.

Potential applications of these types of support conditions in biomechanical modeling clearly extend much beyond the specific modeling topic considered in this paper. They have already been successfully validated, in particular, as boundary conditions in complete heart beat simulations (Chabinok et al. 2009). Further natural applications include the modeling of the attachments of coronary arteries within the

myocardium—a moving support in this case—and the modeling of the effect of intracranial structures and cerebrospinal fluid on the cerebral arteries.

**Acknowledgments** J-F. Gerbeau thanks the Farhat Research Group (Stanford University) for their intellectual hospitality and acknowledges partial support by the Office of Naval Research under Grant N00014-06-1-0505 and Grant N00014-09-C-015.

## References

- Alastrué V, Garcia A, Peña E, Rodríguez JF, Martínez MA, Doblaré M (2010) Numerical framework for patient-specific computational modelling of vascular tissue. *Int J Numer Methods Biomed Eng* 26(1):35–51
- Bertoglio C, Fernández M, Gerbeau J-F, Moireau P (2009) Filtering-based data assimilation in fluid-structure interaction: towards personalization of vascular models. In: Nithiarasu P, Löhner R (eds) 1st International conference on mathematical and computational biomedical engineering—CMBE
- Blanco PJ, Feijóo RA, Urquiza SA (2007) A unified variational approach for coupling 3D-1D models and its blood flow applications. *Comput Methods Appl Mech Eng* 196(41–44):4391–4410
- Blanco PJ, Pivello MR, Urquiza SA, Feijóo RA (2009) On the potentialities of 3D–1D coupled models in hemodynamics simulations. *J Biomech* 42(7):919–930
- Chabiniok R, Chapelle D, Lesault PF, Rahmouni A, Deux JF (2009) Validation of a biomechanical heart model using animal data with acute myocardial infarction. In: CI2BM09–MICCAI workshop on cardiovascular interventional imaging and biophysical modelling, London, UK
- Chen CH, Nevo E, Fetis B, Pak PH, Yin FC, Maughan WL, Kass DA (1997) Estimation of central aortic pressure waveform by mathematical transformation of radial tonometry pressure. validation of generalized transfer function. *Circulation* 95(7):1827–1836
- Ciarlet PG (1988) Mathematical elasticity. Vol. I, volume 20 of *Studies in Mathematics and its Applications*. North-Holland Publishing Co, Amsterdam
- Fernández MA, Gerbeau J-F (2009) *Fluid structure interaction problems in haemodynamics*, chap 9. In: Formaggia L, Quarteroni A, Veneziani A (eds) *Mathematical Modelling of the Cardiovascular System*, Springer, Berlin
- Fernández MA, Gerbeau J-F, Grandmont C (2006) A projection algorithm for fluid-structure interaction problems with strong added-mass effect. *C R Acad Sci Paris Math* 342
- Fernández MA, Gerbeau J-F, Grandmont C (2007) A projection semi-implicit scheme for the coupling of an elastic structure with an incompressible fluid. *Int J Numer Methods Eng* 69(4):794–821
- Figueroa CA, Vignon-Clementel IE, Jansen KE, Hughes TJR, Taylor CA (2006) A coupled momentum method for modeling blood flow in three-dimensional deformable arteries. *Comput Methods Appl Mech Eng* 195(41–43):5685–5706
- Formaggia L, Gerbeau J-F, Nobile F, Quarteroni A (2001) On the coupling of 3D and 1D Navier-Stokes equations for flow problems in compliant vessels. *Comput Methods Appl Mech Eng* 191(6–7):561–582
- Formaggia L, Moura A, Nobile F (2007) On the stability of the coupling of 3D and 1D fluid-structure interaction models for blood flow simulations. *M2AN Math Model Numer Anal* 41(4):743–769
- Fung Y (1993) *Biomechanics: mechanical properties of living tissues*, 2nd edn. Springer, Berlin
- Gee M, Förster C, Wall W (2010) A computational strategy for pre-stressing patient-specific biomechanical problems under finite deformation. *Int J Numer Methods Biomed Eng* 26(1):52–72
- Hauret P, Le Tallec P (2006) Energy-controlling time integration methods for nonlinear elastodynamics and low-velocity impact. *Comput Methods Appl Mech Eng* 195(37–40):4890–4916
- Holzappel GA (2006) Determination of material models for arterial walls from uniaxial extension tests and histological structure. *J Theor Biol* 238(2):290–302
- Humphrey JD (2003) Continuum biomechanics of soft biological tissues. *Proc R Soc Lond A* 459:3–46
- Kerckhoffs RCP, Neal ML, Gu Q, Bassingthwaite JB, Omens JM, McCulloch AD (2007) Coupling of a 3D finite element model of cardiac ventricular mechanics to lumped systems models of the systemic and pulmonary circulation. *Ann Biomed Eng* 35(1):1–18
- Kim HJ, Figueroa CA, Hughes TJR, Jansen KE, Taylor CA (2009) Augmented lagrangian method for constraining the shape of velocity profiles at outlet boundaries for three-dimensional finite element simulations of blood flow. *Comput Methods Appl Mech Eng*
- Kim HJ, Vignon-Clementel IE, Figueroa CA, LaDisa JF, Jansen KE, Feinstein JA, Taylor CA (2009) On coupling a lumped parameter heart model and a three-dimensional finite element aorta model. *Ann Biomed Eng* 37(11):2153–2169
- Le Tallec P (1994) Numerical methods for nonlinear three-dimensional elasticity. In: *Handbook of numerical analysis*, vol III. North-Holland, pp 465–622
- Les AS, Shadden SC, Figueroa CA, Park JM, Tedesco MM, Herfkens RJ, Dalman RL, Taylor CA (2010) Quantification of hemodynamics in abdominal aortic aneurysms during rest and exercise using magnetic resonance imaging and computational fluid dynamics. *Ann Biomed Eng* 38(4):1288–1313
- Moireau P, Chapelle D (2010) Reduced-order unscented Kalman filtering with application to parameter identification in large-dimensional systems. *Cont Optim Calc Variat* [Epub ahead of print]
- Moireau P, Chapelle D, Le Tallec P (2008) Joint state and parameter estimation for distributed mechanical systems. *Comput Methods Appl Mech Eng* 197:659–677
- Moireau P, Chapelle D, Le Tallec P (2009) Filtering for distributed mechanical systems using position measurements: Perspectives in medical imaging. *Inverse Probl* 25(3):035010 (25pp)
- Papadakis G (2009) Coupling 3D and 1D fluid-structure-interaction models for wave propagation in flexible vessels using a finite volume pressure-correction scheme. *Commun Numer Methods Eng* 25(5):533–551
- Sainte-Marie J, Chapelle D, Cimrman R, Sorine M (2006) Modeling and estimation of the cardiac electromechanical activity. *Comput Struct* 84:1743–1759
- Spilker RL, Taylor CA (2010) Tuning multidomain hemodynamic simulations to match physiological measurements. *Ann Biomed Eng* 38(8):2635–2648
- Taylor CA, Figueroa CA (2009) Patient-specific modeling of cardiovascular mechanics. *Annual review of biomedical engineering*, vol 11. Annual reviews, pp 109–134
- Taylor CA, Hughes TJR, Zarins CK (1998) Finite element modeling of blood flow in arteries. *Comput Methods Appl Mech Eng* 158:155–196
- Vignon-Clementel IE, Figueroa CA, Jansen KE, Taylor CA (2006) Outflow boundary conditions for three-dimensional finite element modeling of blood flow and pressure in arteries. *Comput Methods Appl Mech Eng* 195(29–32):3776–3796
- Vignon-Clementel IE, Figueroa CA, Jansen KE, Taylor CA (2010) Outflow boundary conditions for 3D simulations of non-periodic blood flow and pressure fields in deformable arteries. *Comput Methods Biomech Biomed Eng*

- Weiss B, Spahn DR, Rahmig H, Rohling R, Pasch T (1996) Radial artery tonometry: moderately accurate but unpredictable technique of continuous non-invasive arterial pressure measurement. *Br J Anaesth* 76(3):405–411
- Whiting C, Jansen K (2001) A stabilized finite element method for the incompressible Navier-Stokes equations using a hierarchical basis. *Int J Numer Methods Fluids* 35:93–116
- Xiong G, Figueroa CA, Xiao N, Taylor CA (2010) Simulation of blood flow in deformable vessels using subject-specific geometry and assigned variable mechanical wall properties. *Int J Numer Methods Biomed Eng* (Published online)
- Yushkevich PA, Piven J, Hazlett HC, Smith RG, Ho S, Gee JC, Gerig G (2006) User-guided 3d active contour segmentation of anatomical structures: Significantly improved efficiency and reliability. *Neuroimage* 31(3):1116–1128